Chemical Engineering Journal 512 (2025) 162563

Contents lists available at ScienceDirect

Chemical Engineering Journal

journal homepage: www.elsevier.com/locate/cej

Ambient-temperature α-pinene hydrogenation to *cis*-pinane over Ru/CeO$_2$-H catalyst via the dimethyl-up configuration

Yu-Xuan Fu [a], Shu-Yi Huang [a], Ming-Shuai Sun [a,*], Yan Zhou [a], Dan-Dan Cai [a], Wen-Shuai Zhu [a,b,*], Wei Hui [a,b], Duan-Jian Tao [a,*]

[a] *National Engineering Research Center for Carbohydrate Synthesis, Key Laboratory of Fluorine and Silicon for Energy Materials and Chemistry of Ministry of Education, School of Chemical Engineering, Jiangxi Normal University, Nanchang 330022, China*

[b] *College of Chemical Engineering and Environment, State Key Laboratory of Heavy Oil Processing, China University of Petroleum-Beijing, Beijing 102249, China*

ARTICLE INFO

Keywords:
α-pinene
Cis-pinane
Selective hydrogenation
Ru
CeO$_2$

ABSTRACT

Current industrial catalysts for α-pinene hydrogenation suffer from harsh reaction conditions and poor selectivity to *cis*-pinane, primarily due to their inability to effectively adsorb α-pinene in a specific favorable configuration on the catalyst surface. In this study, a high-specific-surface-area, rod-shaped CeO$_2$-supported ultra-fine Ru nanoparticle (average particle size of 4 nm) catalyst was synthesized via hydrothermal method for the highly stereoselective hydrogenation of α-pinene to *cis*-pinane. The resulting Ru/CeO$_2$-H catalyst achieved an α-pinene conversion of 99.3 % and an impressive *cis*-pinane selectivity of up to 99.6 % under exceptionally low temperature (30 °C, 0.6 MPa H$_2$ and 0.5 h with high TOF of 1236 h^{-1}). Density functional theory (DFT) calculations indicated that α-pinene preferentially adsorbs onto the Ru surface via the backside of its intramolecular dimethyl bridge. This particular adsorption mode lowers the energy barriers for further hydrogenation to generate *cis*-pinane. The oriented dimethyl-up configuration of α-pinene and ultra-low activation energy (12.04 kJ/mol obtained from kinetic tests) enable the highly selective production of *cis*-pinane at ambient temperature. Furthermore, the strong interaction between the CeO$_2$-H support and highly dispersed Ru, combined with the ambient-temperature reaction conditions, effectively prevents metal nanoparticle agglomeration and coking, imparting the catalyst with exceptional stability. Notably, the catalyst was reused at least 15 times without observing any significant deactivation, demonstrating its significant potential for practical applications.

1. Introduction

Turpentine oil represents a valuable biomass resource, with α-pinene making up about 80 % of its composition. This compound can be converted into various high-value chemicals, such as synthetic fragrances and pharmaceuticals [1–5]. A key transformation in maximizing the value of turpentine is the hydrogenation of α-pinene to *cis*-pinane. However, this reaction generally produces two isomeric products: *cis*-pinane and *trans*-pinane as shown in Scheme 1 [6–8]. Notably, *cis*-pinane not only demonstrates greater reactivity but also experiences fewer side reactions in the synthesis of downstream high-value chemicals, establishing it as the ultimate desired product in the hydrogenation process of α-pinene [9–11].

In industrial applications, the hydrogenation of α-pinene is typically carried out utilizing Raney nickel (Ni) catalyst under high temperature and pressure conditions (100 ~ 160 °C, 2.0 ~ 2.5 MPa H$_2$). However, concerns over the flammability of Raney Ni have driven researchers to explore safer and more efficient alternative catalysts for this reaction. Noble metals such as palladium (Pd), platinum (Pt), rhodium (Rh), and ruthenium (Ru) are among the most widely studied options. While Pd is known for its high reactivity, it often achieves less than 90 % selectivity for *cis*-pinane due to the random stereochemical adsorption of α-pinene [12–15]. In contrast, Pt and Rh offer better selectivity but at significantly higher costs, thereby increasing catalyst preparation expenses [11,16]. Ru, being a more affordable noble metal than Pd, Pt, and Rh, has gained attention for its remarkable α-pinene conversion and impressive selectivity for *cis*-pinane [17]. For instance, Xie et al. utilized ruthenium nanoparticles stabilized by modified carboxymethyl cellulose to facilitate the hydrogenation of α-pinene in an aqueous solution. Under conditions of 75 °C and 1.5 MPa H$_2$ for 5 h, this method achieved an α-pinene conversion of 96.6 % and a *cis*-pinane selectivity of 98.4 % [18]. Furthermore, Xie's team also reported a surface-modified

---

* Corresponding author.
E-mail addresses: msh_sun@jxnu.edu.cn (M.-S. Sun), zhuws@cup.edu.cn (W.-S. Zhu), djtao@jxnu.edu.cn (D.-J. Tao).

https://doi.org/10.1016/j.cej.2025.162563
Received 27 November 2024; Received in revised form 3 March 2025; Accepted 10 April 2025

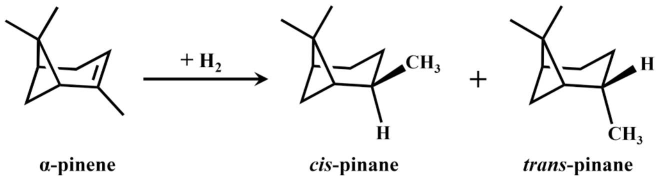

Scheme 1. Hydrogenation of α-pinene to produce *cis*-pinane and *trans*-pinane.

molecular sieve supported Ru nanoparticles, which successfully catalyzed the selective hydrogenation of α-pinene under mild conditions (25 °C, 1 MPa H_2, and 1 h), resulting in complete conversion of α-pinene with a *cis*-pinane selectivity of 99 %. Unfortunately, this catalyst exhibited a significant loss of activity after six recycling cycles [19]. Alain Roucoux stabilized ruthenium nanoparticles in aqueous media using ammonium salt surfactants to catalyze the selective hydrogenation of α-pinene. Under conditions of 110 °C and 3.0 MPa H_2 for 4 h, this approach achieved 100 % conversion of α-pinene with a *cis*-pinane selectivity of 98 % [20]. Despite these advances, challenges remain with coordination agents-stabilized Ru nanoparticles, such as difficulties in product separation and stabilizer loss. Utilizing appropriate carriers to disperse and stabilize Ru nanoparticles could help mitigate these issues; however, supported Ru catalysts still face significant obstacles concerning high reaction temperatures, pressures, and overall stability.

Selecting an appropriate carrier is crucial for optimizing the performance of nanometal catalysts. Cerium dioxide (CeO_2) stands out for its unique ability to transition between Ce^{4+} and Ce^{3+}, which creates abundant oxygen vacancies on its surface and fosters strong interactions with metal nanoparticles [21–23]. This robust metal-O-Ce interface enhances metal dispersion on CeO_2, while its strong adhesion to various metals, including silver (Ag), gold (Au), and platinum (Pt), significantly mitigates or even prevents metal sintering [24–27]. Such fascinating properties of CeO_2 establish favorable conditions for the development of finely dispersed nanometal catalysts. For example, Zhang et al. demonstrated the semi-hydrogenation of quinoline at room temperature using a Pt-CeO_2 catalyst, highlighting the importance of strong electron-metal support interactions [28]. Given its rich oxygen vacancy, strong metal interactions, and controllable synthesis, CeO_2 is emerging as a pivotal support in heterogeneous catalysis. The effective dispersion of Ru on CeO_2 for the selective hydrogenation of α-pinene further underscores its substantial application potential.

In this study, CeO_2 with a large specific surface area was prepared using a straightforward hydrothermal method. Subsequently, metal Ru nanoparticles were supported on CeO_2 to serve as a catalyst for the selective hydrogenation of α-pinene under mild temperature and pressure conditions. The resulting catalyst exhibited excellent reactivity, high *cis*-pinane selectivity, and recycling stability during operation. Additionally, the underlying mechanisms responsible for the catalyst's high activity and selectivity in the production of *cis*-pinane were investigated through a combination of kinetic analysis and density functional theory (DFT) calculations.

2. Experimental section

2.1. Materials

α-Pinene (99 %), $Ce(NO_3)_3·6H_2O$ (99.99 %), $RuCl_3·3H_2O$, NaOH (99 %), methanol (≥99.5 %), ethanol (≥99.5 %), and palladium acetate (99 %) were obtained from Shanghai Titan Scientific Co., Ltd. Commercial Pd/C and Pt/C catalysts were sourced from Shanghai Aladdin Biochemical Technology Co., Ltd. H_2 with a purity of 99.99 % was supplied by Jiangxi Huahong Gas Co., Ltd. All chemicals were utilized as received, without any further treatment.

2.2. Catalyst preparation

Preparation of Ru/CeO_2-H, CeO_2-H550, and CeO_2-H750: First, the carrier CeO_2-H was prepared by a hydrothermal method reported previously [29,30]. Initially, 50 mL aqueous solution containing 14.4 g NaOH was gradually added to 10 mL aqueous solution containing 1.3 g $Ce(NO_3)_3·6H_2O$. The mixture was stirred for 1 h, after which it was transferred to a 100 mL hydrothermal reactor and maintained at a constant temperature of 100 °C for 24 h. The resulting precipitate was washed with deionized water until neutral pH was achieved. Subsequently, the sample was vacuum-dried at 60 °C for 12 h and then calcined in a muffle furnace at 550 °C in an air atmosphere for 4 h to obtain the CeO_2-H carrier, where H stands for the hydrothermal synthesis method. To prepare the Ru/CeO_2-H catalyst, 0.3 g CeO_2-H carrier was impregnated in 33 mL ethanol solution of ruthenium chloride at a concentration of 1 mg/mL. The mixture was stirred for 12 h, after which the solvent was removed using a rotary evaporator. The resultant sample was then reduced in a 10 % H_2/N_2 atmosphere at 550 °C for 6 h with a heating rate of 2.5 °C/min, yielding the CeO_2-H supported Ru catalyst, designated as Ru/CeO_2-H. CeO_2-H550 and CeO_2-H750 was obtained by reducing the bare CeO_2-H support in a 10 % H_2/N_2 atmosphere for 6 h with a heating rate of 2.5 °C/min at 550 °C and 750 °C, respectively.

Preparation of Ru/CeO_2-H750: The preparation of Ru/CeO_2-H750 followed the same procedure as Ru/CeO_2-H, with the sole modification being the reducing temperature using H_2/N_2, which was increased to 750 °C.

Preparation of Ru/CeO_2-C and CeO_2-C550: The CeO_2-C carrier was produced by directly calcining $Ce(NO_3)_3·6H_2O$ at 550 °C for 4 h in a muffle furnace under an air atmosphere. The procedure for loading ruthenium and the theoretical metal loading amount were consistent with those applied for the Ru/CeO_2-H catalyst. The final obtained catalyst was designated as Ru/CeO_2-C, where C stands for the calcination process. CeO_2-C550 was obtained by reducing the bare CeO_2-C support in a 10 % H_2/N_2 atmosphere for 6 h with a heating rate of 2.5 °C/min at 550 °C.

Preparation of Pd/CeO_2-H: In a typical procedure, 0.3 g of CeO_2-H carrier was impregnated with 33 mL of an acetonitrile solution containing 1 mg/mL of palladium acetate, followed by stirring for 12 h. The solvent was then removed using a rotary evaporator, and the obtained solid was subjected to reduction at 550 °C in a 10 % H_2/N_2 atmosphere for 6 h in a tubular furnace, with a heating rate of 2.5 °C/min. The resulting catalyst, denoted as Pd/CeO_2-H, had a theoretical Pd loading of 5 wt%.

2.3. Catalyst characterization

The N_2 adsorption–desorption isotherms of the catalysts were obtained using a Micromeritics Tristar II 3020 instrument, allowing for the assessment of specific surface area, pore size, and pore volume. Prior to analysis, all catalyst samples were evacuated at 100 °C under vacuum for 12 h to eliminate moisture and any potential adsorbed impurities. The crystallographic properties of the catalysts were characterized by X-ray diffraction (XRD) employing Cu Kα radiation ($\lambda = 1.5406$ Å) on a Rigaku RINT-2200 diffractometer, with a scanning speed of 10°/min and over a scanning angle range of 5° to 90°. The morphology and structure were analyzed using a HITACHI SU8020 scanning electron microscope (SEM) and a JEOL JEM-2100 transmission electron microscope (TEM). Elemental distribution was further investigated using energy dispersive spectroscopy (EDS). The hydrogen temperature-programmed reduction (H_2-TPR) analysis was performed using a Micromeritics Auto Chem II 2920 analyzer. All samples underwent pretreatment in a pure He flow at 150 °C for 1 h to remove moisture and any possible adsorbed surface impurities, followed by cooling to 70 °C. The temperature was then ramped to 800 °C at a rate of 10 °C/min in a 10 % H_2/Ar flow, with the detection signal recorded throughout the process. Additionally, the surface elemental composition and chemical states of the catalysts were analyzed using X-ray photoelectron spectroscopy (XPS) under vacuum conditions of 5.0×10^{-8} Pa, employing an AXIS Supra spectrometer (Kratos Analytical Ltd., UK) equipped with a monochromatic Al Kα X-ray source (1486.6 eV). Survey scans were conducted over a binding energy range of 0 ~ 1200 eV, followed by high-resolution scans of specific elements, including C 1s, O 1s, Ru 3d, and Ce 3d, to elucidate the elemental composition and chemical states. The acquired spectra were calibrated using the C 1s peak at 284.8 eV as a reference. The deposition of carbon species on the catalyst was quantitatively analyzed using a thermogravimetric-mass spectrometry (TG-MS) system, specifically a Hitachi 7300 mass spectrometer (MSAA SPECTROMETER LC-D200M PRO, Japan). Approximately 10 mg of the catalyst sample was accurately weighed and placed in a platinum crucible for analysis. The measurement was conducted under an oxygen atmosphere with a flow rate of 50 mL/min. The sample was heated from room temperature to 800 °C at a constant heating rate of 10 °C/min to monitor the thermal processes. Simultaneously, mass spectrometry was employed to detect and analyze the evolved gaseous products during the whole process.

2.4. Catalyst evaluation

In a typical selective hydrogenation process of α-pinene, 0.2 g of α-pinene, 20.0 mg of catalyst, and 6.0 mL of solvent methanol were loaded into a 25 mL stainless steel high-pressure reactor. The reactor was then purged with pure H_2 for 10 min to remove any air, followed by pressurization with H_2 to 0.6 MPa. The reaction was maintained at 30 °C for 2 h with stirring at a speed of 600 rpm. After completion of the reaction, the reactor was cooled to room temperature, and the reaction mixture was filtered and analyzed using gas chromatography. A Thermo Trace 1310 gas chromatograph (Thermo Fisher Scientific, USA) equipped with a TG-5HT capillary column (30 m × 0.25 mm × 0.1 μm, Thermo Fisher Scientific, USA) was used for analysis. The inlet temperature was maintained at 250 °C, and the detector was set to 260 °C. The initial oven temperature was set at 50 °C and held for 1 min, followed by a ramp of 10 °C/min up to 170 °C, with an additional hold time of 2 min at this temperature. The quantitative analysis of post-reaction mixtures was conducted using an internal standard method. *n*-Heptane was employed as the internal standard to ensure accurate quantification. The concentration of α-pinene and each product was determined by gas chromatography (GC), with the response factors calibrated. The peak areas of the target compounds were normalized against the internal standard to calculate their respective concentrations.

The definitions of α-pinene conversion (X), selectivity to *cis*-pinane (S_{cis}), and molar turnover frequency (TOF) are defined as following:

$$X = \frac{C_0 - C}{C_0} \times 100\%$$

$$S_{cis} = \frac{C_{cis}}{C_0 - C} \times 100\%$$

$$\mathrm{TOF} = \frac{n_0 - n}{n_{\mathrm{Ru}} \times t}$$

where C_0 is the initial concentration of α-pinene (mol·L^{-1}), C is the concentration of α-pinene at reaction time t (h), C_{cis} is the concentrations of *cis*-pinane, n_0 is the initial molar amount of α-pinene (mol) added to the reactor, n is the number of moles of α-pinene remained after reaction, and n_{Ru} is the total molar amount of Ru in the catalyst introduced into the reaction system (determined by ICP analysis). Accordingly, the unit of TOF is h^{-1}.

To evaluate the stability of the catalyst, after separation and recovery, the catalyst was washed three times with methanol and dried in a vacuum oven at 40 °C for 1 h before proceeding to the next cycle. Given that approximately 3 % of the catalyst is inevitably lost during the recovery process, an equivalent amount of used catalyst (matching the number of previous uses) is added before each subsequent reaction cycle. This approach helps mitigate any potential decrease in activity due to catalyst loss.

2.5. Computational details

Density functional theory (DFT) calculations were performed to investigate the underlying mechanism contributing to the high selectivity for α-pinene on the prepared Ru catalyst, as well as the comparatively lower selectivity observed on the Pd catalyst. All theoretical calculations were conducted using the CASTEP software package [31]. The Generalized Gradient Approximation (GGA) functional in the Perdew-Burke-Ernzerhof (PBE) form was employed throughout the analysis [32–34]. The typical Ru(200) surface was created in a 3 × 3 supercell with a vacuum slab of 15 Å thickness for surface catalytic reaction. The typical (111) surface of Pd was created in a 4 × 4 supercell with the same vacuum slab thickness. A fine convergence tolerance was applied throughout the calculations. All computations utilized a cut-off energy of 400 eV and a Self-Consistent Field (SCF) tolerance of 2.0×10^{-6} eV/atom. A k-point mesh of 2 × 2 × 1 was implemented for all optimizations, and transition states (TS) were located utilizing the Linear Synchronous Transit/Quadratic Synchronous Transit (LST/QST) method [35,36].

2.6. Kinetic study

The hydrogenation kinetics of α-pinene were investigated using a pseudo-first-order kinetic model, with an excess of H_2 maintained throughout the reaction to fulfill the assumptions required for this model. The total reaction rate constant k for the hydrogenation of α-pinene to form pinane (including both *cis*- and *trans*- isomers) was determined by measuring the concentration C of α-pinene at various reaction times t under a specific reaction temperature T. The rate constant k was obtained from the linear relationship of $\ln(C/C_0)$ versus t. The individual rate constants for the formation of *cis*-pinane (k_1) and *trans*-pinane (k_2) were derived based on the characteristics of parallel (competitive) reactions. Furthermore, the total activation energies E_a (for the overall reaction), E_{a1} (for *cis*-pinane), and E_{a2} (for *trans*-pinane) were calculated by fitting the linear plots of $\ln k$, $\ln k_1$, and $\ln k_2$ versus $1/T$, respectively. Above derivation process for the kinetic study has been supplemented in the Supplementary Materials.

3. Results and discussion

3.1. Characterization of catalysts

Fig. 1 presents the TEM images of the Ru/CeO_2-H and Ru/CeO_2-C catalyst, along with the size distribution of Ru nanoparticles on the support. The Ru/CeO_2-H exhibits a long and slender rod-like morphology, with widths ranging from 6 ~ 15 nm and an average width of 9.4 nm. The length of these rods even extends up to 200 nm (Fig. S1 in the Supplementary Materials). SEM-EDS mapping showed elements O, Ce and Ru exist uniformly on the catalyst surface (Fig. S2 in the Supplementary Materials). High-resolution TEM (HRTEM) images (Fig. 1b) reveal the distance between the clear lattice fringes which was measured to be 0.31 nm, corresponding to the interplanar spacing of the $CeO_2(111)$ crystal plane [37–39]. Ru nanoparticles are uniformly dispersed across the CeO_2-H support, exhibiting a size distribution (Fig. 1c) ranging from 2.5 to 5.5 nm, with an average particle size of 4.0 nm. This uniform distribution and small size of metal Ru on CeO_2-H is indicative of a greater exposure of Ru active sites. The Ru/CeO_2-H750 catalyst, reduced at an elevated temperature of 750 °C, preserved the rod-like morphology of the CeO_2 support (Fig. S3 in the Supplementary Materials). However, high-temperature sintering led to an increase in the Ru nanoparticle size, resulting in an average particle diameter of 6.8 nm. In contrast, the CeO_2-C support, obtained through direct calcination

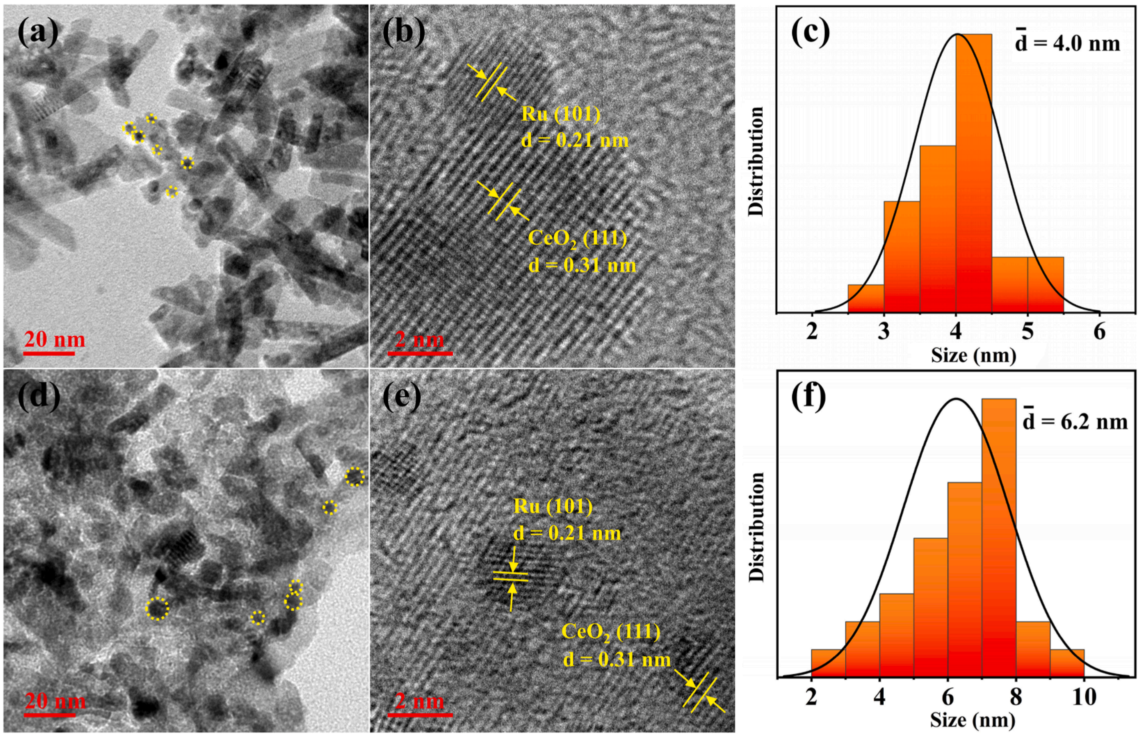

Fig. 1. TEM, HRTEM and Ru particle size distribution images of (a, b, c) Ru/CeO_2-H, and (d, e, f) Ru/CeO_2-C.

of $Ce(NO_3)_3 \cdot 6H_2O$, displays an irregular block-like morphology (Fig. 1d), with the HRTEM image also showing clear lattice fringes with an interplanar spacing of 0.31 nm, corresponding to the CeO_2(1 1 1) crystal plane [39]. TEM images and particle size distribution of the comparative catalyst Pd/CeO_2-H are presented in Fig. S3 (in the Supplementary Materials). It illustrates the characteristic lattice fringes of the Pd(1 1 1) crystal plane, with an interplanar spacing of 0.22 nm [40,41]. In contrast to Ru/CeO_2-H, the Pd nanoparticles on CeO_2-H exhibit a significantly larger size, ranging from 4 nm to 14 nm, with an average particle size of 9.2 nm. This larger size is disadvantageous for the exposure of more active Pd sites.

Fig. 3 displays the N_2 adsorption–desorption isotherms of as-prepared Ru catalysts and CeO_2 supports, and pore diameter distributions are presented in Fig. S4 (in the Supplementary Materials). BET surface area analysis (Table 1) indicates that the hydrothermally prepared CeO_2-H support possesses a significantly higher specific surface area of 162.8 m^2/g, compared to only 48.8 m^2/g for CeO_2-C obtained from the direct calcination of cerium nitrate. After the loading of Ru, the specific surface area of Ru/CeO_2-H remains high at 84.7 m^2/g, which is 1.66 times larger than that of Ru/CeO_2-C (50.9 m^2/g). Furthermore, the pore volume (0.47 cm^3/g) and average pore size (19.35 nm) of Ru/CeO_2-H are considerably higher than those of Ru/CeO_2-C. This substantial specific surface area and rich pore structure facilitate the diffusion of reactants and products, thereby being beneficial for accelerating the chemical reaction rate. Data analysis from Table 1 reveals that the hydrothermally synthesized support CeO_2-H (162.8 m^2/g) experienced a reduction in specific surface area after high-

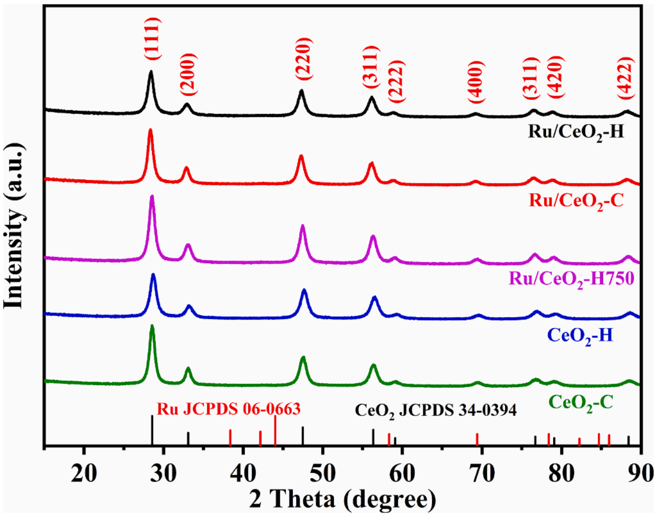

Fig. 2. XRD patterns of as-prepared Ru catalysts and CeO_2 supports.

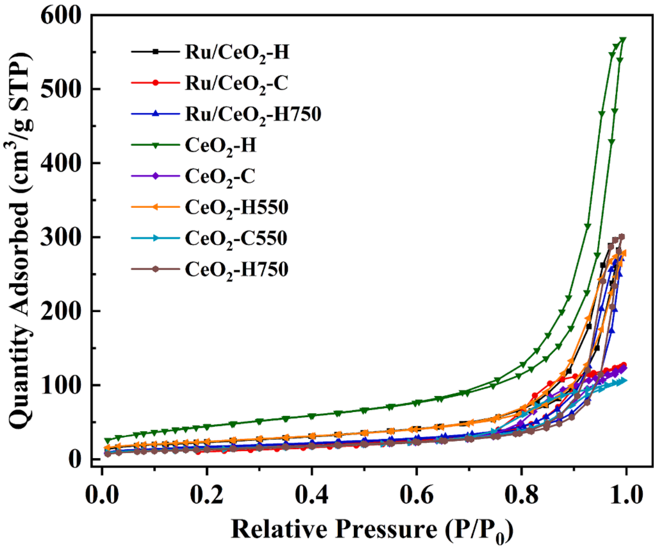

Fig. 3. N_2 adsorption–desorption isotherms of as-prepared Ru catalysts and CeO_2 supports.

Table 1
Textural parameters of the prepared catalysts and supports.

Entry	Sample	S_{BET} (m^2/g)	Pore Volume (cm^3/g)	Pore Size (nm)
1	Ru/CeO_2-H	84.7	0.47	19.35
2	Ru/CeO_2-C	50.9	0.20	10.15
3	Ru/CeO_2-H750	57.3	0.42	26.68
4	CeO_2-H	162.8	0.88	19.23
5	CeO_2-C	48.8	0.19	12.49
6	CeO_2-H550	84.9	0.43	18.16
7	CeO_2-C550	50.1	0.16	11.78
8	CeO_2-H750	49.0	0.46	26.79

temperature treatment in the 10 % H_2/N_2 atmosphere. The samples CeO_2-H550 (84.9 m^2/g) and CeO_2-H750 (49.0 m^2/g) were obtained by treating CeO_2-H at 550 °C and 750 °C for 6 h, respectively. The observed changes in pore volume (0.88 cm^3/g → 0.46 cm^3/g) and pore diameter (19.23 nm → 26.79 nm) suggest that high-temperature treatment led to structural collapse, increasing the pore diameter while decreasing the pore volume. Consequently, the specific surface area of Ru/CeO_2-H (84.7 m^2/g) was nearly identical to that of CeO_2-H550 but lower than that of CeO_2-H, confirming the dominant impact of thermal treatment on the surface area. Compared to high-temperature H_2/N_2 treatment, the influence of Ru metal on the catalyst's surface area is negligible. Further comparative analysis reveals that high-temperature H_2/N_2 reduction leads to an increase in the specific surface area of the CeO_2-C support, exhibiting a completely opposite trend compared to its effect on CeO_2-H. In Table 1 (Entry 2 and 5), it could also be found that the prolonged high-temperature treatment induced structural changes in the framework of CeO_2-C, leading to an increase in pore volume from 0.19 cm^3/g to 0.20 cm^3/g and a decrease in pore diameter from 12.49 nm to 10.15 nm, which contributed to the growth of the specific surface area. The specific surface area of CeO_2-C550 (50.1 m^2/g) was comparable to that of Ru/CeO_2-C (50.9 m^2/g), further supporting the conclusion that high-temperature reduction rather than Ru metal influences the textural properties of the support. The differing structural effects of high-temperature reduction on CeO_2-H and CeO_2-C are likely attributed to the differences in their preparation methods, which inherently influence their structural characteristics.

Fig. 2 displays the XRD patterns of as-prepared Ru-loaded catalysts and the two CeO_2 supports. Clear diffraction peaks corresponding to characteristic crystallographic planes of CeO_2 including (111) (28.6°), (200) (33.1°), and (220) (47.5°) etc. are observed [42,43]. Notably, no discernible diffraction peaks corresponding to Ru are observed in the XRD patterns of Ru/CeO_2-H, Ru/CeO_2-C, or even Ru/CeO_2-H750, which was reduced at a much higher temperature (750 °C). Reducing the scan speed from 5°/min to 1°/min in the narrow 2θ range 35–50° (Fig. S5 in the Supplementary Materials) still did not detect any diffraction peaks corresponding to Ru. The absence of Ru signals in XRD can be attributed to its low content relative to CeO_2 or the small particle size of Ru on average, which limits the diffraction intensity. ICP analysis (Table S1) determined that the Ru content in the catalyst ranged from 2.4 to 3.0 wt %. Given the particularly small Ru particle size, the characteristic diffraction peaks of Ru may be challenging to detect in the XRD analysis. This aligns with the TEM analysis, where Ru nanoparticles are visible with clear lattice fringes but small size in average. In the XRD pattern of Pd/CeO_2-H (Fig. S6 in the Supplementary Materials), alongside the characteristic peaks of CeO_2, a faint diffraction signal at 40.1° corresponding to the Pd(111) crystalline plane is observed [44,45]. This weak diffraction intensity is likely due to the small particle size of Pd and its relatively low loading content.

Fig. 4 presents the FTIR spectra of the three Ru-based catalysts. A broad peak around 3446 cm^{-1} corresponds to typical bridging hydroxyl groups [46]. Near 1630 cm^{-1}, a band is attributed to the bending vibration of hydroxyl groups associated with adsorbed water [47]. The peak at 1384 cm^{-1} also corresponds to –OH vibrations, as reported in the literature [48]. A small peak around 1314 cm^{-1} is linked to Ce–O–Ce vibrations, while broad peaks near 700 cm^{-1} and 500 cm^{-1} serve as fingerprints for Ce–O bonds [48,49]. These surface functional group characteristics are consistent with most reported CeO_2 supports, indicating the successful synthesis of the CeO_2 support.

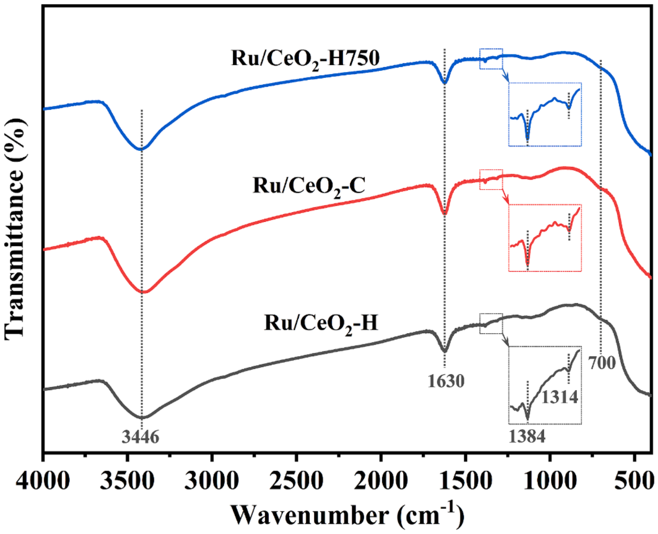

Fig. 4. FTIR spectra of the prepared Ru catalysts.

The valence states and surface compositions of the prepared Ru catalysts were characterized by XPS. Fig. 5 presents the Ru 3d and Ce 3d spectra of the three Ru-based catalysts, and Table 2 summarizes the percentages of Ru^0, oxygen vacancies (O_β), and Ce^{3+} species. Deconvolution of the Ru $3d_{5/2}$ spectra identified three valence states, with binding energy peaks located at approximately 280.5 eV (Ru^0), 281.5 eV (Ru^{4+}), and 282.8 eV (Ru^{6+}) (Fig. 5a) [50–52]. As shown in Table 2, the surface Ru^0 content of the three catalysts varies slightly, with values of 56 % for Ru/CeO_2-H, 52 % for Ru/CeO_2-C, and 58 % for Ru/CeO_2-H750. The Ce 3d spectra were deconvoluted into ten peaks. The peaks at approximately 880.4 eV and 885.0 eV ($3d_{5/2}$), along with their corresponding $3d_{3/2}$ peaks, were assigned to Ce^{3+} species, while the remaining six peaks were attributed to Ce^{4+} species [50–53]. The Ce^{3+} content (Table 2) follows the trend Ru/CeO_2-H < Ru/CeO_2-C < Ru/CeO_2-H750. The O 1s spectra (presented in Fig. S7 in the Supplementary Materials) were deconvoluted into three peaks at approximately 529.5 eV, 531.2 eV, and 533.0 eV, corresponding to lattice oxygen, oxygen vacancies, and surface-adsorbed oxygen species, respectively [50,52–54]. Oxygen vacancies were detected on all three Ru-supported catalysts, which are critical for stabilizing metallic Ru on the catalyst surface. A comparison between Ru/CeO_2-H and Ru/CeO_2-H750 indicates that higher reduction temperatures promote oxygen loss from the CeO_2 lattice, resulting in the formation of oxygen vacancies and Ce^{3+} species, consistent with previous studies [51,55,56]. However, despite having the highest oxygen vacancy content, Ru/CeO_2-H750 exhibited inferior catalytic performance compared to Ru/CeO_2-H. This observation suggests that, beyond oxygen vacancy content, the highly dispersed state of metallic Ru on the support surface is a more decisive factor in achieving superior catalytic performance.

H_2-TPR analyses were conducted to investigate the redox properties of the Ru-based catalysts and CeO_2 supports, as illustrated in Fig. 6. The reduction peak observed below 180 °C corresponds to RuO_x species. Notably, Ru/CeO_2-H exhibits the lowest reduction temperature (115 °C), indicating the most potent reducibility and the strongest H_2 dissociation capability among the three Ru catalysts [57]. The RuO_x reduction temperature in Ru/CeO_2-C, at 125 °C, is slightly higher, positioning it as the second most reducible. Differently, Ru species in Ru/CeO_2-C show the highest reduction temperatures, with two peaks

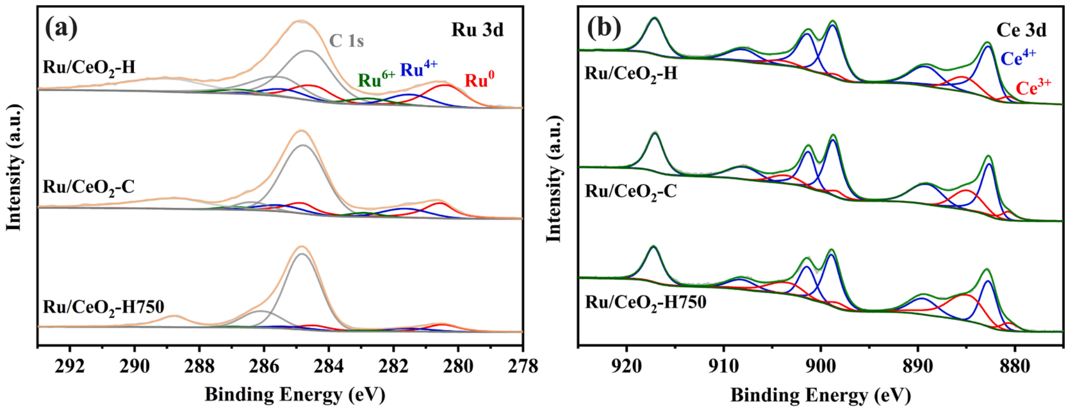

Fig. 5. XPS spectra of (a) Ru 3d and (b) Ce 3d for as-prepared Ru catalysts.

Table 2
Surface content of Ce, O and Ru species on the prepared Ru catalysts.

Sample	Surface content (%)							
	Ce^{3+}	Ce^{4+}	O_α	O_β	O_γ	Ru^0	Ru^{4+}	Ru^{6+}
Ru/CeO$_2$-H	12	88	75	16	9	56	28	16
Ru/CeO$_2$-C	20	80	71	22	7	52	37	11
Ru/CeO$_2$-H750	33	67	54	33	13	58	33	9

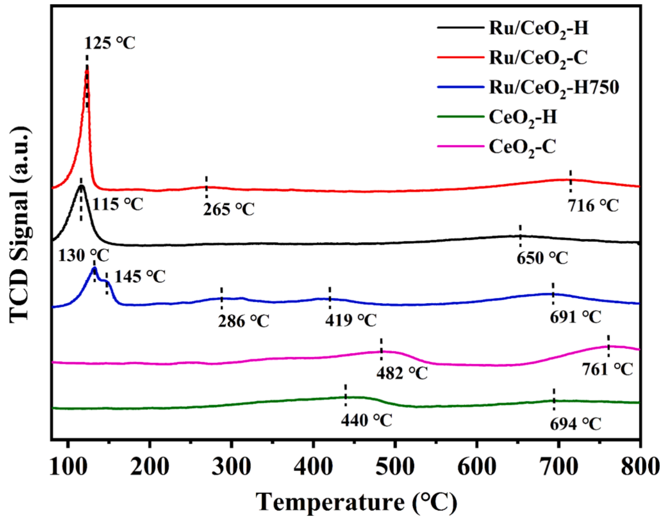

Fig. 6. H_2-TPR of as-prepared Ru catalysts and CeO_2 supports.

below 180 °C. This phenomenon is likely due to the presence of two distinct Ru species formed during high-temperature (750 °C) reduction. One species consists of Ru incorporated into the CeO_2 lattice as Ru-O-Ce which reduces at a lower temperature, and the other one is RuO_2 located on the support surface, requiring a higher reduction temperature [57–60]. The trend in Ru species reduction temperatures (Ru/CeO$_2$-H < Ru/CeO$_2$-C < Ru/CeO$_2$-H750) suggests a descending order of H_2 dissociation capability: Ru/CeO$_2$-H > Ru/CeO$_2$-C > Ru/CeO$_2$-H750, consistent with the catalytic activity reported in Table 3 (Ru/CeO$_2$-H > Ru/CeO$_2$-C > Ru/CeO$_2$-H750). Reduction peaks observed between 180 °C and 600 °C correspond to the reduction of Ce^{4+} to Ce^{3+} [57,58,61], while peaks above 600 °C are attributed to the reduction of bulk ceria, independent of Ru [57,62]. Furthermore, the reduction peaks of Ru-loaded CeO_2 shift to lower temperatures relative to pure CeO_2 [62,63].

Table 3
Catalytic activity of α-pinene hydrogenation and selectivity to *cis*-pinane on different catalysts.

Entry	Catalyst	Reaction condition	Conversion (%)	Selectivity (%)
1	Ru/CeO$_2$-H	30 °C, 0.6 MPa, 2 h	99.3	99.6
2	Ru/CeO$_2$-C	30°C, 0.6 MPa, 2 h	80.2	98.5
3	Ru/CeO$_2$-H750	30°C, 0.6 MPa, 2 h	20.3	97.6
4	Pd/CeO$_2$-H	30°C, 0.6 MPa, 2 h	27.8	67.1
5	Pd/C	30°C, 0.6 MPa, 2 h	99.4	82.4
6	Pt/C	30°C, 0.6 MPa, 2 h	99.4	79.0

3.2. Catalytic performance of catalysts

The catalytic performance of the Ru-based catalysts supported on CeO_2 for the hydrogenation of α-pinene is summarized in Table 3. For comparison, commercial Pd/C and Pt/C catalysts were also evaluated under identical reaction conditions. As illustrated in Table 3, the Ru/CeO$_2$-H catalyst exhibited outstanding performance, achieving an α-pinene conversion of 99.3 % and a *cis*-pinane selectivity of 99.6 % after 2 h under mild reaction conditions (30 °C, 0.6 MPa). In contrast, the Ru/CeO$_2$-C catalyst exhibited significantly lower activity and poor selectivity to *cis*-pinane, with a modest α-pinene conversion of 80.2 % and a *cis*-pinane selectivity of 98.5 % under the same conditions. This pronounced difference in performance can be attributed to the superior physicochemical properties of the CeO$_2$-H support, which was prepared via hydrothermal synthesis. The nanorods have a small size, with diameters ranging from 6 to 15 nm and lengths up to 200 nm as characterized by TEM. This elongated nanostructure inherently lacks large pores. Ru particles are primarily deposited on the surface of the nanorods, and the elongated rod-shaped support can stack and interlace, creating larger and more abundant inter-rod voids. The higher specific surface area, larger pore volume, and pore size of CeO$_2$-H facilitate better dispersion of Ru nanoparticles and enhance the diffusion of reactants and products. These features boost the activity of the catalyst. On catalyst Ru/CeO$_2$-H750, a substantial decline in catalytic activity was observed. The α-pinene conversion sharply declined to 20.3 %, representing a reduction of up to 79 % compared to Ru/CeO$_2$-H, accompanied by a slight decrease in *cis*-pinane selectivity. This reduction in performance is likely due to the aggregation of Ru nanoparticles at elevated reduction temperatures, which leads to a decrease in the number of active Ru sites available on the catalyst surface, thereby seriously weakening catalytic efficiency. Blank reactions for identifying activity of the supports were also carried out under the same reaction conditions as the Ru-based catalysts. It was found that none of the three supports (CeO$_2$-H, CeO$_2$-H550, CeO$_2$-C, CeO$_2$-C550 and CeO$_2$-H750) exhibited catalytic activity, even when the reaction temperature was increased to 120 °C. This confirms that the observed hydrogenation activity originates from the Ru species. Table 2 provides the surface content of various Ru species. The three Ru-based catalysts contain similar amounts of Ru^0, while the Ru^{4+} and Ru^{6+} contents vary. Since olefin hydrogenation is primarily catalyzed by zero-valent metals, Ru should be in the metallic state (Ru^0) to effectively dissociate H_2. Unreduced, high-valent Ru species, such as Ru^{4+} and Ru^{6+} generally lack intrinsic hydrogenation activity. Therefore, Ru^0 serves as the key active species in α-pinene hydrogenation, while Ru^{4+} and Ru^{6+} contribute negligibly to catalytic performance. From the data in Table 2 and Table 3, while it appears that catalysts with higher Ru^{6+} content exhibit higher α-pinene conversion, it is difficult to conclude that an increased Ru^{6+} fraction directly enhances catalytic activity. A more rigorous data analysis reveals a strong linear correlation between Ru nanoparticle size in average and Ru^{6+} content, which is in better agreement than the correlation between Ru^{6+} content and α-pinene conversion. This observation suggests that higher Ru dispersion results in both an increased exposure of Ru^0 active sites and greater interaction between Ru atoms and the CeO_2 support, leading to the formation of high-valent Ru^{6+} species. A more cautious and reasonable conclusion is that the high dispersion of Ru on the CeO_2 surface, which leads to an increased exposure of Ru^0 active sites, is the direct reason for the enhanced catalytic activity. The increase in Ru^{6+} content is merely a consequence of the high dispersion of Ru and does not contribute significantly to catalytic activity.

As reported, oxygen vacancies on CeO_2 usually play a crucial role in activating hydrogen, enhancing hydrogen spillover, improving metal dispersion, or strengthening metal-support interactions [64–66]. However, in the H_2-TPR profiles of blank CeO_2-H and CeO_2-C (Fig. 6), no hydrogen consumption peaks are observed in the low-temperature region (< 300 °C), suggesting that H_2 dissociation is challenging on the prepared blank CeO_2 support by sole oxygen vacancies. Interestingly, after loading Ru, all three catalysts (Ru/CeO_2-H < Ru/CeO_2-C < Ru/CeO_2-H750) exhibit hydrogen consumption peaks at lower temperatures, indicating that Ru plays the key role in hydrogen dissociation. From the TG-MS analysis (Fig. S10 in the Supplementary Materials), a continuous weight loss is found due to hydroxyl condensation dehydration. This suggests that oxygen vacancies interact with the hydrogen spillover produced by Ru during H_2 dissociation to form surface hydroxyl groups, thereby facilitating H–H bond cleavage and hydrogen migration, in line with previous reports [66]. However, no positive correlation is found between catalyst activity and the amount of oxygen vacancies (O_β) from the data in Table 2 and Table 3. It is likely that the increased catalytic activity, resulting from the higher dispersion of Ru and the corresponding increase in metal active sites, outweighs the positive effect brought about by the increased oxygen vacancy content. Thus, it is proposed that the primary role of oxygen vacancies is to improve the dispersion of Ru and enhance metal-support interactions, which exposes more active sites and prevents nanoparticle agglomeration and deactivation of the catalyst.

The catalytic performance of the CeO_2-H-supported Pd catalyst (Pd/CeO_2-H) was notably suboptimal, exhibiting an α-pinene conversion of merely 27.8 % and a *cis*-pinane selectivity of only 67.1 %. In contrast, the commercial Pd/C and Pt/C catalysts demonstrated significantly higher catalytic activity, achieving α-pinene conversions exceeding 99 %. However, their *cis*-pinane selectivity was considerably lower than that of Ru/CeO_2-H, averaging around 80 %. Table S1 (in the Supplementary Materials) further highlights other highly effective α-pinene hydrogenation catalysts reported in the literature, including Ni, Pd, and Rh etc. Comparatively, the Ru/CeO_2-H catalyst distinguishes itself by delivering superior catalytic performance under milder reaction conditions, operating at a temperature of 30 °C and a pressure of 0.6 MPa, which are notably milder than those required for the other catalysts. Additionally, it achieves exceptional α-pinene conversion and *cis*-pinane selectivity.

The effects of reaction temperature, H_2 pressure, and reaction time on the conversion and *cis*-pinane selectivity in the hydrogenation of α-pinene catalyzed by Ru/CeO_2-H were systematically investigated

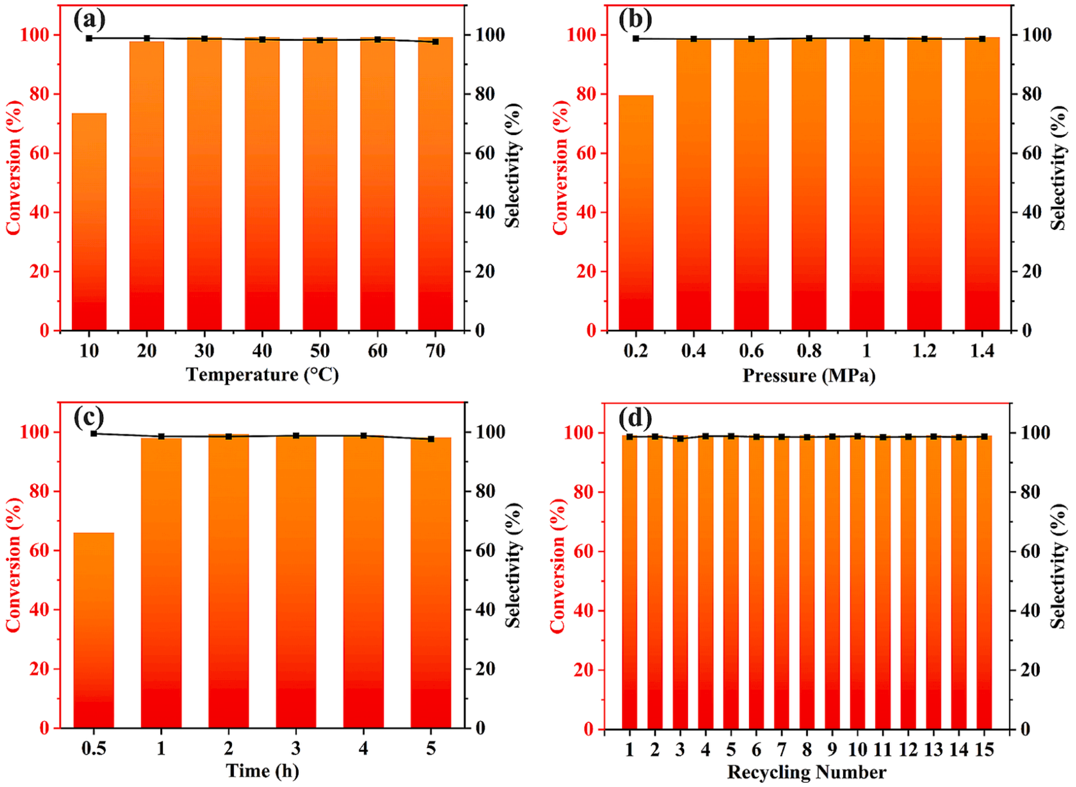

Fig. 7. Catalytic performance and reusability test of α-pinene hydrogenation on Ru/CeO_2-H catalyst. Reaction conditions: (a) 0.2 g substrate, 20 mg catalyst, 6 mL methanol, 0.6 MPa H_2, 600 rpm, 2 h; (b) 0.2 g substrate, 20 mg catalyst, 6 mL methanol, 30 °C, 600 rpm, 2 h; (c) 0.2 g substrate, 20 mg catalyst, 6 mL methanol, 30 °C, 0.6 MPa H_2, 600 rpm; (d) 0.2 g substrate, 20 mg catalyst, 6 mL methanol, 30 °C, 0.6 MPa H_2, 600 rpm, 2 h.

(Fig. 7). In Fig. S8 (in the Supplementary Materials), the exploration of catalyst dosage at 30 °C and 0.6 MPa H_2 revealed that a catalyst-to-substrate (α-pinene) mass ratio of 1:10 was sufficient to achieve complete conversion of α-pinene. Moreover, further increasing the catalyst dosage did not result in a decline in *cis*-pinane selectivity. In the subsequent exploration of temperature, pressure, and other reaction conditions, the same catalyst-to-substrate ratio was maintained. Notably, as the reaction temperature increased from 10 °C to 70 °C, the *cis*-pinane selectivity decreased only slightly, from 99.6 % to 97.7 %. This observation indicates that the selectivity for *cis*-pinane remains exceptionally high, even at elevated temperatures. Moreover, extending the reaction time to 5 h (Fig. 7c) maintained a high *cis*-pinane selectivity of 97.6 %. Increasing the H_2 pressure to 1.4 MPa resulted in a *cis*-pinane selectivity of 98.7 %, with no significant rise in *trans*-pinane selectivity. These findings illustrate that the Ru/CeO_2-H catalyst exhibits remarkable adaptability to variations in reaction conditions—including temperature, H_2 pressure, and reaction time—without a corresponding increase in the yield of the by-product *trans*-pinane under more rigorous conditions. Additionally, the turnover frequency (TOF) for α-pinene hydrogenation over Ru/CeO_2-H reaches 1236 h^{-1} (30 °C, 0.6 MPa H_2 and 0.5 h). This TOF value is markedly higher than those reported for many Ru-based or other metal catalysts (e.g., Ni, Pd, Rh) as listed in Table S2 [10,12,16,67–71].

3.3. Cyclic stability of the catalyst Ru/CeO_2-H

The recycling performance of the Ru/CeO_2-H catalyst in the hydrogenation of α-pinene is presented in Fig. 7d. After 15 cycles, the catalyst maintains a conversion and *cis*-pinane selectivity approaching 100 %, demonstrating exceptional stability throughout the recycling process. X-ray diffraction (XRD) analysis of the recycled catalyst (Fig. S9 in the Supplementary Materials) reveals no detectable diffraction peaks corresponding to Ru, indicating that the Ru nanoparticles have not undergone agglomeration. This observation suggests a strong interaction between the Ru nanoparticles and the CeO_2-H support. Additionally, the mild reaction temperature (30 °C) effectively mitigates the agglomeration of Ru nanoparticles and inhibits the formation of carbon deposits. To further confirm that no carbon deposition occurs, thermogravimetric and mass spectrometry (TG-MS) analysis under an O_2 atmosphere (Fig. S10 in the Supplementary Materials). The results showed that only H_2O was produced throughout the weight loss process. The H_2O signal originated from two sources: water molecules desorbed on the catalyst below 200 °C [72], and water produced by the dehydration of surface hydroxyl groups as the temperature increased [52]. No CO_2 signals were detected at any stage, indicating that no carbon deposition occurred on the catalyst surface. Collectively, these factors contribute to the catalyst's sustained stability and prolonged service life.

3.4. Mechanism of high cis-pinane selectivity on Ru/CeO_2-H

The high selectivity of the Ru/CeO_2-H catalyst for the formation of *cis*-pinane was elucidated through DFT calculations. The reaction pathways for the hydrogenation of α-pinene on the Ru(200) and Pd(111) crystal planes were computed to assess the generation of both *cis*-pinane and *trans*-pinane. The energy changes and corresponding structures for each step of the reaction pathway are illustrated in Fig. S12 ~ S15 (in the Supplementary Materials), respectively. As depicted in Fig. 8a, the adsorption energy of α-pinene on the Ru(200) surface in the dimethyl-up configuration (−0.46 eV) is significantly lower than that in the dimethyl-down configuration (−0.04 eV). This observation suggests a preferential adsorption of α-pinene on the Ru(200) surface with a dimethyl-up orientation, promoting the hydrogenation pathway toward *cis*-pinane formation. Furthermore, the energy barrier for the first hydrogenation step (the addition of an H atom to the C atom of the C=C bond) is 0.4 eV (TS1), which is considerably lower than the energy barrier (0.77 eV) for the first hydrogen addition in the *trans*-pinane formation pathway. Additionally, the energy barrier (TS2) for adding the second H atom in the *cis*-pinane formation process is 0.5 eV, which is lower than the 0.63 eV barrier (TS2) for *trans*-pinane formation. The energy variation pathways for *cis*-pinane and *trans*-pinane formation on the Ru(101) surface have also been calculated, as shown in Fig. S11 (in the Supplementary Materials). The corresponding optimized structures and identified transition states are presented in Fig. S16 and S17 (in the Supplementary Materials). The results reveal that, similar to the Ru (200) surface, α-pinene follows the same adsorption and hydrogenation preference on Ru(101). The activation barriers for this pathway, TS1 (0.79 eV) and TS2 (1.03 eV), are both lower than those for *trans*-pinane formation, where TS1 (1.28 eV) and TS2 (1.80 eV) are observed. α-Pinene predominantly adsorbs in the dimethyl-bridge-up orientation toward *cis*-pinane formation on Ru(101) surface. These findings suggest that α-pinene is preferentially converted to *cis*-pinane via hydrogenation on the Ru catalyst. In contrast, for the comparative catalyst Pd (Fig. 8b), the adsorption energy of α-pinene on the Pd(200) surface in both structural configurations are −0.09 eV, indicating a relatively high degree of randomness in adsorption. On the Pd catalyst, the energy barriers for the hydrogenation of α-pinene to *cis*-pinane are 0.51 eV for the first step (TS1) and 0.64 eV for the second step (TS2). Similarly, the energy barriers for the formation of *trans*-pinane are 0.57 eV for TS1 and 0.67 eV for TS2. The close proximity of these energy barriers suggests that the hydrogenation of α-pinene to produce either *cis*-pinane or *trans*-pinane encounters comparable kinetic challenges on the Pd catalyst. Although the energy barrier for *cis*-pinane formation is marginally lower, the difference is notably less pronounced than that observed with the Ru metal. This aligns with the conclusion that the Ru catalyst exhibits significantly higher selectivity for *cis*-pinane, whereas selectivity on the Pd catalyst is markedly reduced.

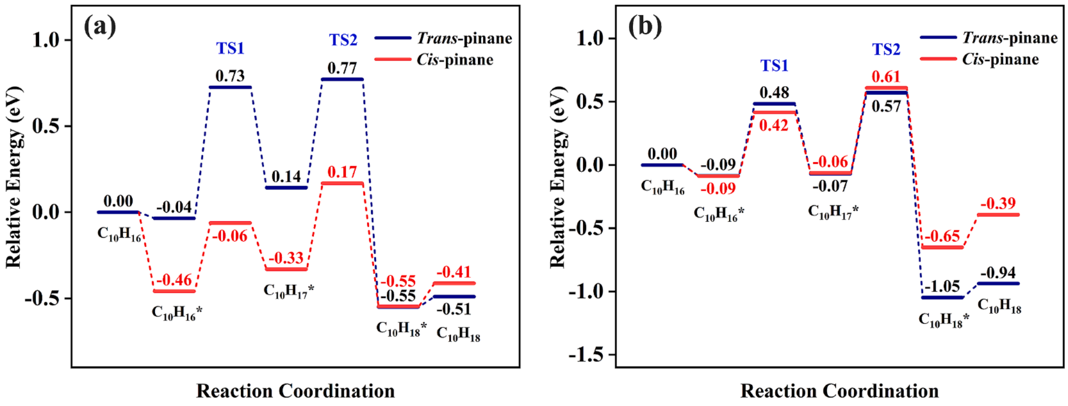

Fig. 8. Relative energy profiles of α-pinene hydrogenation to produce *cis*-pinane and *trans*-pinane on (a) Ru(200) and Pd(111) surface.

3.5. Kinetic study

The hydrogenation kinetics of α-pinene over Ru/CeO_2-H were thoroughly examined, with a particular emphasis on activation energy at low reaction temperature. To ensure a stable hydrogen concentration in the reaction medium, an excess of H_2 was supplied by maintaining a high pressure of 1.0 MPa with a continuous feed, enabling the reaction to be approximated as a pseudo-first-order process. Kinetic studies were conducted at 30 °C, 40 °C, and 50 °C (as shown in Fig. 9a), yielding rate constant k for the overall hydrogenation of α-pinene to *cis*-pinane and *trans*-pinane of 0.01522 min^{-1}, 0.01758 min^{-1}, and 0.02083 min^{-1}, respectively. The overall activation energy for the transformation of α-pinene, calculated using the Arrhenius equation, was notably low at 12.44 kJ·mol^{-1}. Reaction rate constants k_1 and k_2 at different temperatures were listed in Table S3 (in the Supplementary Materials). Following a parallel reaction model, the plot of the natural logarithm of the rate constant (ln k_1) for the hydrogenation of α-pinene to *cis*-pinane versus 1/T (Fig. 9c) provided an activation energy of 12.04 kJ·mol^{-1}, aligning closely with the overall activation energy for the process. In comparison, the activation energy (E_a) for the formation of *trans*-pinane was found to be 27.41 kJ·mol^{-1}, which is substantially higher than the E_a for *cis*-pinane formation, indicating a preferential facilitation by the Ru/CeO_2-H catalyst toward *cis*-pinane production. Moreover, the energy barrier for *cis*-pinane formation on Ru/CeO_2-H is significantly lower than that reported for the Pd/Al_2O_3 (28 ± 3 kJ/mol), Pd/C (35.5 ± 1.4 kJ/mol) and Ni-B alloy (68.2 kJ/mol) catalysts [13,15,73]. This is also the critical factor enabling Ru/CeO_2-H to achieve efficient hydrogenation of α-pinene under ambient temperature conditions. These kinetic results demonstrate strong agreement with both DFT calculations and experimental data, underscoring the selective efficacy of Ru/CeO_2-H in the hydrogenation of α-pinene to produce *cis*-pinane at impressively mild conditions.

4. Conclusions

In summary, we have successfully developed a novel Ru-based catalyst that efficiently catalyzes the highly selective hydrogenation of α-pinene to *cis*-pinane under ambient temperature with high efficiency. The rod-like CeO_2, with its large specific surface area and strong support-metal interactions, enhances the dispersion of Ru nanoparticles, significantly boosting catalytic activity. These mild conditions also prevent carbon deposition, contributing to the catalyst's excellent cyclic stability. Mechanistic studies reveal that α-pinene preferentially adsorbs onto the catalyst surface via the backside of its intramolecular dimethyl bridge, which lowers the hydrogenation energy barrier and promotes the selective formation of *cis*-pinane. Moreover, kinetic analysis demonstrates that the activation energy for the hydrogenation of α-pinene to *cis*-pinane on this Ru-based catalyst is substantially lower than that for *trans*-pinane formation. Overall, the catalyst exhibits outstanding performance, including high activity under mild conditions, exceptional selectivity, and robust stability over multiple cycles, showcasing its immense potential for industrial applications.

CRediT authorship contribution statement

Yu-Xuan Fu: Investigation, Formal analysis. **Shu-Yi Huang:** Visualization. **Ming-Shuai Sun:** Writing – original draft, Software, Data curation, Writing – review & editing. **Yan Zhou:** Validation. **Dan-Dan Cai:** Validation. **Wen-Shuai Zhu:** Resources, Methodology. **Wei Hui:** Supervision, Investigation. **Duan-Jian Tao:** Writing – original draft, Resources, Project administration, Funding acquisition, Conceptualization, Writing – review & editing.

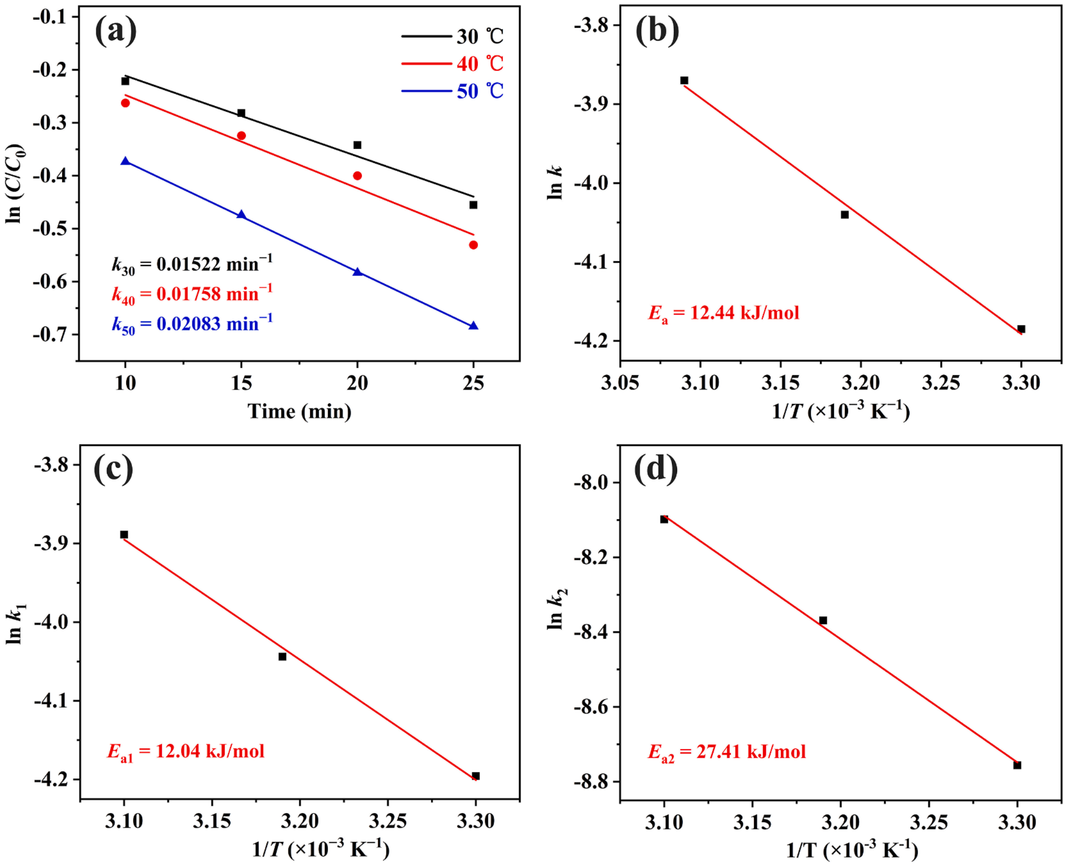

Fig. 9. Kinetic studies of α-pinene hydrogenation. Reaction conditions: substrate (0.30 g), Ru/CeO_2-H catalyst (10 mg), methanol (30 mL), H_2 pressure (1.0 MPa).

Declaration of competing interest

The authors declare that they have no known competing financial interests or personal relationships that could have appeared to influence the work reported in this paper.

Acknowledgments

We thank the National Natural Science Foundation of China (22378178); the Natural Science Foundations of Jiangxi Province (20242BAB25156).

Appendix A. Supplementary data

Supplementary data to this article can be found online at https://doi.org/10.1016/j.cej.2025.162563.

Data availability

Data will be made available on request.

References

[1] L. Frattini, M.A. Isaacs, C.M.A. Parlett, K. Wilson, G. Kyriakou, A.F. Lee, Support enhanced α-pinene isomerization over HPW/SBA-15, Appl Catal B 200 (2017) 10–18.

[2] M. Akgül, B. Özyağcı, A. Karabakan, Evaluation of Fe- and Cr-containing clinoptilolite catalysts for the production of camphene from α-pinene, J. Ind. Eng. Chem. 19 (2013) 240–249.

[3] M. Liu, X. Zhao, Z. Ma, B. Yuan, F. Yu, C. Xie, S. Yu, An alkylation route for developing novel liquid aviation fuels from α-pinene and mixed isobutane/isobutene, Chem. Eng. Sci. 281 (2023) 119174.

[4] B. Yuan, Z. Wang, X. Yue, F. Yu, C. Xie, S. Yu, Biomass high energy density fuel transformed from α-pinene catalyzed by Brönsted-Lewis acidic heteropoly inorganic-organic salt, Renew. Energy 123 (2018) 218–226.

[5] D. Yin, Z. Hu, M. Liu, J. Zhang, H. Zheng, Y. Hou, S. Yu, L. Li, S. Liu, Y. Liu, Highly stereoselective hydrogenation of αpinene over Ir nanoparticles confined in SiO_2 shells, Chem. Eng. J. 484 (2024) 149374.

[6] W. Lai, J. Lu, Z. Shi, F. Lei, W. Qi, J. Yang, Z. Xing, A. Wu, L. Shen, Thermal isomerism and pyrolysis mechanism of α-pinene and β-pinene in a solvent-free solution and ethanol based on density functional theory, Chem. Phys. 544 (2021) 111103.

[7] D. Chouchi, D. Gourgouillon, M. Courel, J. Vital, M. Nunes da Ponte, The Influence of Phase Behavior on Reactions at Supercritical Conditions: The Hydrogenation of α-Pinene, Ind. Eng. Chem. Res. 40 (2001) 2551–2554.

[8] A. Milewska, A.M.B. Osuna, I.M. Fonseca, M.N. da Ponte, Biphasic hydrogenation of α-pinene in high-pressure carbon dioxide, Green Chem. 7 (2005) 726–732.

[9] D. Kinzel, A. Stolle, B. Ondruschka, L. González, Quantum chemical investigation of the thermal rearrangement of *cis*- and *trans*-pinane, PCCP 12 (2010) 9884–9892.

[10] X. Wang, F. Yu, C. Xie, S. Yu, Highly selective hydrogenation of α-pinene in aqueous medium using PVA-stabilized Ru nanoparticles, Mol. Catal. 444 (2018) 62–69.

[11] S. Hou, J. Dong, Z. Zhu, L. Geng, Y. Ma, B. Zhao, Size-Tunable Ultrafine Pt Nanoparticles in Soluble Metal–Organic Cages: Displaying Highly Stereoselective Hydrogenation of α-Pinene, Chem. Mater. 32 (2020) 7063–7069.

[12] F.J. Ndongou Moutombi, A. Selka, A.-S. Fabiano-Tixier, D. Foucher, O. Clarisse, F. Chemat, M. Touaibia, Highly selective solvent-free hydrogenation of pinenes to added-value cis-pinane, C. r. Chim. 21 (2018) 1035–1042.

[13] I.L. Simakova, Y. Solkina, I. Deliy, J. Wärnå, D.Y. Murzin, Modeling of kinetics and stereoselectivity in liquid-phase α-pinene hydrogenation over Pd/C, Appl. Catal. A 356 (2009) 216–224.

[14] Y. Yang, X. Liu, D. Yin, Z. Zhang, D. Lei, J. Yang, A recyclable Pd colloidal catalyst for liquid phase hydrogenation of α-pinene, J. Ind. Eng. Chem. 26 (2015) 333–334.

[15] F. Yu, Y. Shi, F. Wu, B. Yuan, C. Xie, S. Yu, Aqueous-phase hydrogenation of α-pinene catalyzed by Ni-B alloys loaded on a Janus amphiphilic carbon@silica nanomaterial, Ind. Crop. Prod. 185 (2022) 115140.

[16] X. Chen, B. Yuan, F. Yu, Y. Liu, C. Xie, S. Yu, Hydrogenation of α-Pinene over Platinum Nanoparticles Reduced and Stabilized by Sodium Lignosulfonate, ACS Omega 5 (2020) 8902–8911.

[17] C. Xie, L. Qu, H. Yu, F. Yu, B. Yuan, S. Yu, S. Nie, Synthesis of Ru nanoparticles with hydroxyethyl cellulose as stabilizer for high-efficiency reduction of α-pinene, Cellul. 26 (2019) 8059–8071.

[18] L. Qu, H. Yu, F. Yu, B. Yuan, C. Xie, S. Yu, Catalytic reduction of α-pinene using Ru nanoparticles stabilized by modified carboxymethyl cellulose, Appl. Surf. Sci. 453 (2018) 271–279.

[19] F. Yu, L. Xie, F. Wu, B. Yuan, C. Xie, S. Yu, X. Liu, L. Wang, D. Wang, Mild Hydrogenation of α-Pinene Catalyzed by Ru Nanoparticles Loaded on Boron-doped Amphiphilic Core-Shell Mesoporous Molecular Sieves, ChemCatChem 11 (2019) 1518–1525.

[20] M. Duval, S. Navarre, G. Sagorin, A. Denicourt-Nowicki, A. Roucoux, Multigram Scale-up of the Selective Hydrogenation of α-Pinene with Ruthenium Nanoparticles in Water, ACS Sustain. Chem. Eng. 8 (2020) 5985–5993.

[21] F. Esch, S. Fabris, L. Zhou, T. Montini, C. Africh, P. Fornasiero, G. Comelli, R. Rosei, Electron Localization Determines Defect Formation on Ceria Substrates, Science 309 (2005) 752–755.

[22] C.T. Campbell, C.H.F. Peden, Oxygen Vacancies and Catalysis on Ceria Surfaces, Science 309 (2005) 713–714.

[23] H. Yan, N. Zhang, D. Wang, Highly efficient CeO_2-supported noble-metal catalysts: From single atoms to nanoclusters, Chem Catal. 2 (2022) 1594–1623.

[24] Y. Zhang, S. Zhao, J. Feng, S. Song, W. Shi, D. Wang, H. Zhang, Unraveling the physical chemistry and materials science of CeO_2-based nanostructures, Chem 7 (2021) 2022–2059.

[25] J.A. Farmer, C.T. Campbell, Ceria Maintains Smaller Metal Catalyst Particles by Strong Metal-Support Bonding, Science 329 (2010) 933–936.

[26] N. Ta, J. Liu, S. Chenna, P.A. Crozier, Y. Li, A. Chen, W. Shen, Stabilized Gold Nanoparticles on Ceria Nanorods by Strong Interfacial Anchoring, J. Am. Chem. Soc. 134 (2012) 20585–20588.

[27] J. Zhang, D. Zhu, J. Yan, C. Wang, Strong metal-support interactions induced by an ultrafast laser, Nat. Commun. 12 (2021) 6665.

[28] S. Zhang, Z. Xia, T. Ni, Z. Zhang, Y. Ma, Y. Qu, Strong electronic metal-support interaction of Pt/CeO_2 enables efficient and selective hydrogenation of quinolines at room temperature, J. Catal. 359 (2018) 101–111.

[29] H. Mai, L. Sun, Y. Zhang, R. Si, W. Feng, H. Zhang, H. Liu, C. Yan, Shape-Selective Synthesis and Oxygen Storage Behavior of Ceria Nanopolyhedra, Nanorods, and Nanocubes, J. Phys. Chem. B 109 (2005) 24380–24385.

[30] Y. Li, Z. Wei, F. Gao, L. Kovarik, C.H.F. Peden, Y. Wang, Effects of CeO_2 support facets on VO_x/CeO_2 catalysts in oxidative dehydrogenation of methanol, J. Catal. 315 (2014) 15–24.

[31] S.J. Clark, M.D. Segall, C.J. Pickard, P.J. Hasnip, M.I.J. Probert, K. Refson, M. C. Payne, First principles methods using CASTEP, Zeitschrift Für Kristallographie - Crystalline Materials 220 (2005) 567–570.

[32] W. Kohn, L.J. Sham, Self-consistent equations including exchange and correlation effects, Phys. Rev. 140 (1965) A1133.

[33] J.P. Perdew, K. Burke, M. Ernzerhof, Generalized gradient approximation made simple, Phys. Rev. Lett. 77 (1996) 3865.

[34] G. Kresse, D. Joubert, From ultrasoft pseudopotentials to the projector augmented-wave method, Phys. Rev. B 59 (1999) 1758.

[35] T.A. Halgren, W.N. Lipscomb, The synchronous-transit method for determining reaction pathways and locating molecular transition states, Chem. Phys. Lett. 49 (1977) 225–232.

[36] N. Govind, M. Petersen, G. Fitzgerald, D. King-Smith, J. Andzelm, A generalized synchronous transit method for transition state location, Comput. Mater. Sci 28 (2003) 250–258.

[37] G. Wang, Q. Mu, T. Chen, Y. Wang, Synthesis, characterization and photoluminescence of CeO_2 nanoparticles by a facile method at room temperature, J. Alloy. Compd. 493 (2010) 202–207.

[38] Y. Guo, Y. Qin, H. Liu, H. Wang, J. Han, X. Zhu, Q. Ge, CeO_2 Facet-Dependent Surface Reactive Intermediates and Activity during Ketonization of Propionic Acid, ACS Catal. 12 (2022) 2998–3012.

[39] X. Wang, D. Liu, S. Song, H. Zhang, Pt@CeO_2 Multicore@Shell Self-Assembled Nanospheres: Clean Synthesis, Structure Optimization, and Catalytic Applications, J. Am. Chem. Soc. 135 (2013) 15864–15872.

[40] Y. Feng, Q. Shao, Y. Ji, X. Cui, Y. Li, X. Zhu, X. Huang, Surface-modulated palladium-nickel icosahedra as high-performance non-platinum oxygen reduction electrocatalysts, Sci. Adv. 4 (2018) eaap8817.

[41] W. Zhu, S. Kattel, F. Jiao, J.G. Chen, Shape-Controlled CO_2 Electrochemical Reduction on Nanosized Pd Hydride Cubes and Octahedra, Adv. Energy Mater. 9 (2019) 1802840.

[42] H. Zhao, P. Cao, L. Lu, F. Li, C.H. Pang, T. Wu, Co-regulation of dispersion, exposure and defect sites on CeO_2 (111) surface for catalytic oxidation of Hg^0, J. Hazard. Mater. 424 (2022) 126566.

[43] F. Jiang, S. Wang, B. Liu, J. Liu, L. Wang, Y. Xiao, Y. Xu, X. Liu, Insights into the Influence of CeO_2 Crystal Facet on CO_2 Hydrogenation to Methanol over Pd/CeO_2 Catalysts, ACS Catal. 10 (2020) 11493–11509.

[44] M. Cheng, P. Lv, X. Zhang, R. Xiong, Z. Guo, Z. Wang, Z. Zhou, M. Zhang, A new active species of Pd-N_x synthesized by hard-template method for efficiently catalytic hydrogenation of nitroarenes, J. Catal. 399 (2021) 182–191.

[45] D. Wu, K. Deng, B. Hu, Q. Lu, G. Liu, X. Hong, Plasmon-Assisted Photothermal Catalysis of Low-Pressure CO_2 Hydrogenation to Methanol over Pd/ZnO Catalyst, ChemCatChem 11 (2019) 1598–1601.

[46] N. Vardast, M. Haghighi, H. Zeinalzadeh, Catalytic properties/performance evolution during sono-hydrothermal design of nanocrystalline ceria over zinc oxide for biofuel production, Chem. Eng. J. 430 (2022) 132764.

[47] C. Rodríguez, C. Castañeda, E. Sosa, J.J. Martínez, S. Mancipe, H. Rojas, F. Tzompantzi, R. Gómez, Enhanced Photocatalytic Degradation of Herbicide 2,4-Dichlorophenoxyacetic Acid Using Sulfated CeO_2, Catalysts 14 (2024) 594.

[48] A. Ansari, A. Kaushik, Synthesis and optical properties of nanostructured $Ce(OH)_4$, J. Semicond. 31 (3) (2010) 033001, https://doi.org/10.1088/1674-4926/31/3/033001.

[49] M. Farahmandjou, M. Zarinkamar, Synthesis of nano-sized ceria (CeO_2) particles via a cerium hydroxy carbonate precursor and the effect of reaction temperature on particle morphology, Journal of Ultrafine Grained and Nanostructured Materials 48 (2015) 5–10.

[50] H. Huang, Q. Dai, X. Wang, Morphology effect of Ru/CeO_2 catalysts for the catalytic combustion of chlorobenzene, Appl. Catal. B 158 (2014) 96–105.

[51] X. Qin, X. Chen, M. Chen, J. Zhang, H. He, C. Zhang, Highly efficient Ru/CeO_2 catalysts for formaldehyde oxidation at low temperature and the mechanistic study, Cat. Sci. Technol. 11 (2021) 1914–1921.

[52] B. Lin, B. Fang, Y. Wu, C. Li, J. Ni, X. Wang, J. Lin, C.-T. Au, L. Jiang, Enhanced ammonia synthesis activity of ceria-supported ruthenium catalysts induced by CO activation, ACS Catal. 11 (2021) 1331–1339.

[53] C. Li, M. Li, Y. Zheng, B. Fang, J. Lin, J. Ni, B. Lin, L. Jiang, Revealing hydrogen migration effect on ammonia synthesis activity over ceria-supported Ru catalysts, Appl. Catal. B 320 (2023) 121982.

[54] L. Shi, Y.-K. Liao, Y.-H. Dong, Y.-A. Wang, Y. Zhou, X.-G. Yi, M.-S. Sun, W. Hui, D.-J. Tao, Hollow branched fiber hierarchical porous carbon as recyclable adsorbents and catalysts for efficient CO2 capture and conversion, Sustain. Mater. Technol. 40 (2024) e00880.

[55] K. Wang, Y. Chang, L. Lv, Y. Long, Effect of annealing temperature on oxygen vacancy concentrations of nanocrystalline CeO_2 film, Appl. Surf. Sci. 351 (2015) 164–168.

[56] T. Montini, M. Melchionna, M. Monai, P. Fornasiero, Fundamentals and catalytic applications of CeO_2-based materials, Chem. Rev. 116 (2016) 5987–6041.

[57] S. López-Rodríguez, A. Davó-Quiñonero, E. Bailón-García, D. Lozano-Castelló, A. Bueno-López, Effect of Ru loading on Ru/CeO_2 catalysts for CO_2 methanation, Mol. Catal. 515 (2021) 111911.

[58] D. Fu, X. Wu, B. Cui, Y. Guo, H. Wang, J. Han, Q. Ge, X. Zhu, $Ru_{0.05}Ce_{0.95}O_2$ Solid Solution Derived Ru Catalyst Enables Selective Hydrodeoxygenation of m-Cresol to Toluene, ChemCatChem 13 (2021) 4814–4823.

[59] J.-H. Park, T.-S. Chang, Promotional Effect of Ruthenium Addition to Co/α-Al_2O_3 Catalyst for Dry Reforming of Methane, Catal. Lett. 149 (2019) 3148–3159.

[60] F. Wang, C. Li, X. Zhang, M. Wei, D.G. Evans, X. Duan, Catalytic behavior of supported Ru nanoparticles on the 100}, {110}, and {111 facet of CeO2, J. Catal. 329 (2015) 177–186.

[61] S. Lu, Y. Jing, S. Jia, M. Shakouri, Y. Hu, X. Liu, Y. Guo, Y. Wang, Enhanced Production of Liquid Alkanes from Waste Polyethylene via the Electronic Effect-Favored Csecondary−Csecondary Bond Cleavage, ChemCatChem 15 (2023) e202201375.

[62] Z. Ma, S. Zhao, X. Pei, X. Xiong, B. Hu, New insights into the support morphology-dependent ammonia synthesis activity of Ru/CeO_2 catalysts, Cat. Sci. Technol. 7 (2017) 191–199.

[63] T. Sakpal, L. Lefferts, Structure-dependent activity of CeO_2 supported Ru catalysts for CO_2 methanation, J. Catal. 367 (2018) 171–180.

[64] K. Werner, X. Weng, F. Calaza, M. Sterrer, T. Kropp, J. Paier, J. Sauer, M. Wilde, K. Fukutani, S. Shaikhutdinov, H.-J. Freund, Toward an Understanding of Selective Alkyne Hydrogenation on Ceria: On the Impact of O Vacancies on H_2 Interaction with CeO_2(111), J. Am. Chem. Soc. 139 (2017) 17608–17616.

[65] K. Zheng, Y. Li, B. Liu, F. Jiang, Y. Xu, X. Liu, Ti-doped CeO_2 Stabilized Single-Atom Rhodium Catalyst for Selective and Stable CO_2 Hydrogenation to Ethanol, Angew. Chem. Int. Ed. 61 (2022) e202210991.

[66] Q. Zhang, X. Liao, S. Liu, H. Wang, Y. Zhang, Y. Zhao, Tuning Particle Sizes and Active Sites of Ni/CeO_2 Catalysts and Their Influence on Maleic Anhydride Hydrogenation, Nanomaterials 12 (2022) 2156.

[67] M. Bao, F. Yu, B. Yuan, C. Xie, S. Yu, Aqueous-phase hydrogenation of α-pinene to *cis*-pinane using an amphiphilic Ni-based catalyst, BioResources (2023).

[68] S. Liu, F. Yu, B. Yuan, C. Xie, S. Yu, Ru-Ni Alloy Nanoparticles Loaded on N-Doped Amphiphilic Mesoporous Hollow Carbon@silica Spheres as Catalyst for the Hydrogenation of α-Pinene to *cis*-Pinane, ChemPlusChem (2023) e202200443.

[69] Q. Liu, G. Yang, B. Zhang, F. Zhang, X. Jiang, S. Liu, New core-shell catalyst for catalyzing hydrogenation of α-pinene to *cis*-pinane, Fuel 361 (2024) 130662.

[70] P. Huang, Q. Deng, L. Jiang, Y. Zhi, W. Yang, J. Huang, Y. Zheng, Y. Wang, S. Shan, T. Hu, H. Su, The Exploration of Sensitive Factors for the Selective Hydrogenation of α-Pinene Over Recyclable Ni-B/KIT-6 Catalyst, Catal. Lett. 152 (2022) 2352–2365.

[71] F. Wu, F. Yu, B. Yuan, C. Xie, S. Yu, Highly selective and recyclable hydrogenation of α-pinene catalyzed by ruthenium nanoparticles loaded on amphiphilic core–shell magnetic nanomaterials, Appl. Organomet. Chem. 33 (2019) e5165.

[72] Q. Wu, X. Chen, J. Mi, S. Cai, L. Ma, W. Zhao, J. Chen, J. Li, The Absence of Oxygen in Sulfation Promotes the Performance of the Sulfated CeO_2 Catalyst for Low-Temperature Selective Catalytic Reduction of NO^x by NH_3: Redox Property versus Acidity, ACS Sustain. Chem. Eng. 9 (2021) 967–979.

[73] I.I. Il'ina, I.L. Simakova, V.A. Semikolenov, Kinetics of the Hydrogenation of α-Pinene to *cis*- and *trans*-Pinanes on Pd/C, Kinet. Catal. 43 (2002) 645–651.